LETTER

doi:10.1038/nature25010

Structures of β-klotho reveal a 'zip code'-like mechanism for endocrine FGF signalling

Sangwon Lee[1], Jungyuen Choi[1], Jyotidarsini Mohanty[1], Leiliane P. Sousa[1], Francisco Tome[1], Els Pardon[2], Jan Steyaert[2], Mark A. Lemmon[1], Irit Lax[1] & Joseph Schlessinger[1]

Canonical fibroblast growth factors (FGFs) activate FGF receptors (FGFRs) through paracrine or autocrine mechanisms in a process that requires cooperation with heparan sulfate proteoglycans, which function as co-receptors for FGFR activation[1,2]. By contrast, endocrine FGFs (FGF19, FGF21 and FGF23) are circulating hormones that regulate critical metabolic processes in a variety of tissues[3,4]. FGF19 regulates bile acid synthesis and lipogenesis, whereas FGF21 stimulates insulin sensitivity, energy expenditure and weight loss[5]. Endocrine FGFs signal through FGFRs in a manner that requires klothos, which are cell-surface proteins that possess tandem glycosidase domains[3,4]. Here we describe the crystal structures of free and ligand-bound β-klotho extracellular regions that reveal the molecular mechanism that underlies the specificity of FGF21 towards β-klotho and demonstrate how the FGFR is activated in a klotho-dependent manner. β-Klotho serves as a primary 'zip code'-like receptor that acts as a targeting signal for FGF21, and FGFR functions as a catalytic subunit that mediates intracellular signalling. Our structures also show how the sugar-cutting enzyme glycosidase has evolved to become a specific receptor for hormones that regulate metabolic processes, including the lowering of blood sugar levels. Finally, we describe an agonistic variant of FGF21 with enhanced biological activity and present structural insights into the potential development of therapeutic agents for diseases linked to endocrine FGFs.

We used X-ray crystallography to determine the structure of the free and ligand-bound extracellular region of human β-klotho (sKLB) (Extended Data Fig. 1, Methods), in order to elucidate the mechanism of action of β-klotho in cell signalling via FGF21 stimulation. The overall structure of sKLB (2.2 Å resolution, Extended Data Table 1) features two tandem glycoside hydrolase-like domains, D1 (residues 53–507) and D2 (residues 521–968), which are connected by an unstructured and flexible linker (Fig. 1a). Each glycoside hydrolase-like domain can be recognized by multiple repeats of alternating layers of β-sheet and α-helix that define the $(\beta/\alpha)_8$ fold (Extended Data Fig. 2a). The structure of KLB_{D1} (1.7 Å resolution, Extended Data Table 1) shown in Fig. 1b is virtually identical to the structure of D1 in the context of sKLB, with an overall C_α root mean square deviation (r.m.s.d.) value of 0.48 Å. Four loop regions in the structure of sKLB that contain potential *N*-glycosylation sites could not be modelled owing to poor electron density: a loop between H0 and S1 (residues 63–73; H denotes α-helix and S denotes β-sheet), a loop between H1b and H1c (residues 119–125), a loop between S9 and H9a (residues 538–574) and the C terminus of the protein (residues 968–983) (Extended Data Fig. 2a). With the exception of the C terminus, these loops are depicted in the sKLB structures as dashed lines (Fig. 1a).

Superimposing the structure of human cytosolic β-glucosidase (RCSB Protein Data Bank (PDB) code: 2ZOX) on the structures of each of the two glycoside hydrolase-like domains in sKLB gave C_α r.m.s.d. values of 1.08 Å for D1 and 1.39 Å for D2, respectively, which demonstrates the strong similarity of both D1 and D2 to glycoside hydrolase family-1 (GH1) enzymes (Fig. 1d, e). GH1 enzymes hydrolyse glycosidic linkages between carbohydrate moieties (http://www.cazy.org/GH1.html) through a double-replacement mechanism mediated by two conserved glutamate residues located in their active sites[6]. In each of the sKLB domains, one of these two 'catalytic' glutamates is replaced by another amino acid (Fig. 1d–f): the first glutamate in D1 is replaced by Asn241, and the second glutamate in D2 is replaced by Ala889. This indicates that neither glycoside hydrolase-like domain in β-klotho can function as an active glycoside-hydrolase enzyme. Structural alignment using the Dali server[7] indicates that GH1 and GH5 members exhibit high structural similarities to each of the glycoside hydrolase-like domains of sKLB, suggesting a common evolutionary origin. Although the overall structures of the glycoside hydrolase-like domains in sKLB are very similar to GH1 enzymes, the two sKLB glycoside hydrolase-like domains exhibit important structural features that set them apart from GH1 enzymes.

The pocket in D1 that corresponds to the substrate-binding region in GH1 enzymes is largely occluded by a short helix, H6a (Fig. 1d and Extended Data Fig. 3a). Moreover, a helix-turn-strand element (H6a-turn-S6b) in this region, specific to β-klotho D1 (green in Fig. 1d), provides part of the FGF21-binding site (see below) and is quite distinct from the strand-helix-strand element in the corresponding regions of cytosolic β-glucosidase (shown in grey in Fig. 1d). Other features unique to β-klotho include a short helix, H0 (Fig. 1d and Extended Data Fig. 3b), which begins with the first amino acid that follows the sKLB signal sequence (Phe53). This helix interacts with H5a, H6b and S5b, mostly through hydrophobic interactions, and precedes a disordered loop that is followed by the core structural elements of the $(\beta/\alpha)_8$ fold. Glu416, the remaining catalytic residue in D1, is located at the bottom of the substrate-binding pocket (Fig. 1d and Extended Data Fig. 3a), and the orientation of the side chain of Glu416 is identical to the orientation of the side chain of the corresponding nucleophilic Glu373 residue of human cytosolic β-glucosidase.

The pocket in D2 that corresponds to the substrate-binding pocket in GH1 enzymes is not occluded by an α-helix in the D2 domain, but is instead accessible and occupied by a 2-(*N*-morpholino)ethanesulfonic acid (MES) molecule from the crystallization buffers (Fig. 1c). The morpholine ring of MES interacts with aromatic rings from three phenylalanines, Phe931, Phe826 and Phe942 (Fig. 1c), which also have a role in the interaction of sKLB with its ligands (see below). The D2 pocket is accessible in part because of the existence of a disordered region between S9 and H9a (Extended Data Fig. 2a), which produces a groove-like feature in this domain instead of the pocket that accommodates the substrate in the active site of GH1 members. The amino acid sequence and the length of this region vary considerably among GH1 members. The inter-domain interface of sKLB comprises an extensive network of both hydrophobic and polar interactions (Extended Data Fig. 3c) that encompasses a buried surface area[8] of about 680 $Å^2$.

[1]Department of Pharmacology and Yale Cancer Biology Institute, Yale School of Medicine, 333 Cedar Street, New Haven, Connecticut 06520, USA. [2]VIB Center for Structural Biology, Vrije Universiteit Brussel, Pleinlaan 2, 1050 Brussels, Belgium.

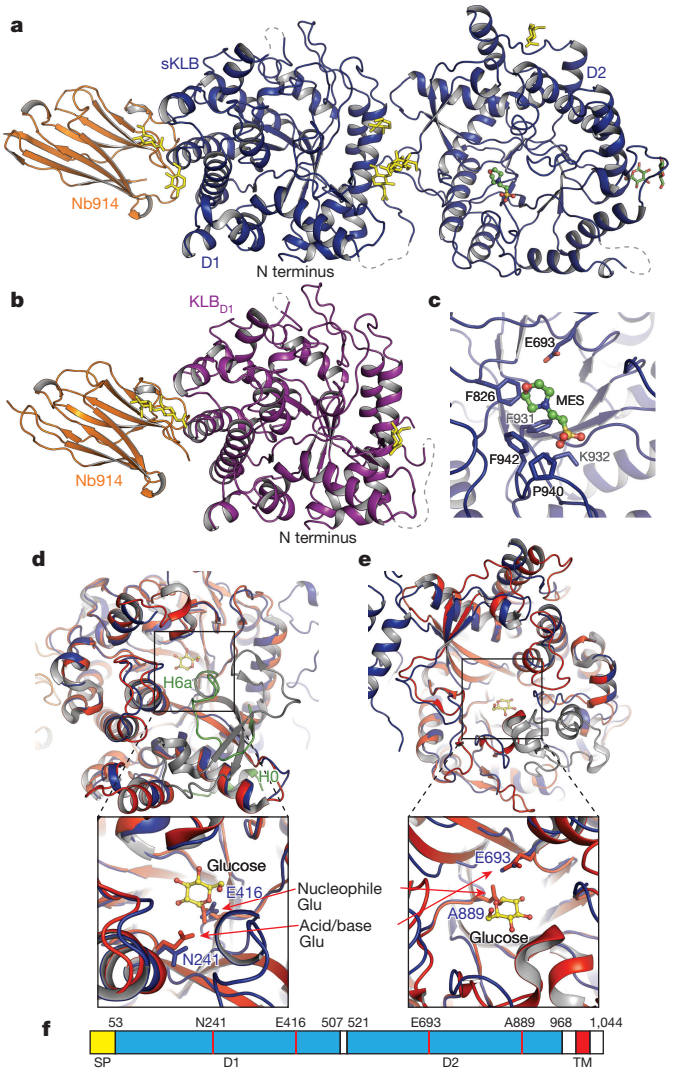

Figure 1 | Crystal structure of extracellular domain of β-klotho. **a**, **b**, Structures of sKLB (**a**) (blue) and KLB$_{D1}$ (**b**) (purple) in complex with nanobody Nb914 (orange) are shown as ribbon representations. Yellow sticks denote glycans attached to asparagine side chains; green sticks denote glucose molecules; the MES molecule is shown as a ball-and-stick representation; dashed grey lines indicate regions that do not show significant electron density. **c**, Side-chain atoms of amino acids in sKLB interacting with the MES molecule are shown as sticks. Also indicated is the location of Glu693, which is approximately 6 Å away from the bound MES molecule. **d**, **e**, The structure of human cytosolic β-glucosidase (red; PDB code: 2ZOX) is superimposed with that of D1 (**d**) and D2 (**e**) of sKLB (blue) with overall C_α r.m.s.d. values of 1.08 Å and 1.39 Å, respectively. Regions in sKLB that are different from β-glucosidase are coloured in green; regions in β-glucosidase that are different from sKLB are coloured in grey. A glucose molecule bound to β-glucosidase is shown as a ball-and-stick representation in yellow. Superimposition of D1 and D2 reveals locations of pseudo-catalytic glutamates. Note that one of the two conserved glutamates from each of the sKLB domains is replaced by an asparagine (for D1) or an alanine (for D2). **f**, Diagram of β-klotho that highlights the locations of the residues corresponding to the conserved glutamates in D1 and D2 of β-klotho. SP, signal peptide, TM, transmembrane.

Next, we determined the structure of sKLB in complex with C-terminal tail of FGF21 (FGF21$_{CT}$) at 2.6 Å resolution (Fig. 2a and Extended Data Table 1). Our final model contains amino acids Pro186–Ser209 from FGF21$_{CT}$ bound to sKLB (Extended Data Fig. 4a–c), and exhibited clear electron density for FGF21$_{CT}$ that lay across the middle of sKLB (Fig. 2b). FGF21$_{CT}$ binds to an elongated interface that spans D1 and D2 of sKLB; this binding has no influence on the structure of either individual domain, as judged by a C_α r.m.s.d. values of 0.33 Å for D1 and 0.49 Å for D2 when overlaid on the unoccupied sKLB structure. We observed a small change of 6° in the inter-domain angle[9] when FGF21$_{CT}$ bound to sKLB (Extended Data Fig. 4d). The FGF21$_{CT}$-binding region on sKLB is located on the opposite side of the molecule from the linker that connects D1 and D2. The flexibility of the linker may contribute to the inter-domain dynamic properties that enable complex formation with ligands and FGFRs. The sKLB–FGF21$_{CT}$ structure shows two distinct binding sites for two different regions of the peptide: site 1 is located on D1 and site 2 is located in D2, with a distance of 30 Å between them.

Site 1 on sKLB D1 engages amino acids Pro186–Val197 of FGF21$_{CT}$, primarily through hydrophobic interactions (Fig. 2e, Extended Data Fig. 4a, b). Site 1 involves a surface created on D1 by H6a, H7, the loop between S6b and H6b, and the loop between S7 and H7. Most notably, the region of the bound peptide ligand that associates with site 1 adopts an unusually compact and rigid structure through the formation of several well-defined turns (Fig. 2e), as follows: (1) Asp187-Val188-Gly189-Ser190 form a type I β-turn (shown in orange in Fig. 2e) through hydrogen bonding of the carboxyl oxygen of Asp187 with the backbone nitrogen of Gly189, and of the backbone carbonyl of Asp176 with the backbone amide of Ser190; (2) Ser190-Ser191-Asp192 form an ST turn (a structural feature containing hydrogen-bonded serine or threonine residues, shown in yellow in Fig. 2e) through hydrogen bonding of the Ser190 hydroxyl with the backbone amide of Asp192; (3) Asp192-Pro193-Leu194-Ser195 (shown in light blue in Fig. 2e) form a type I β-turn (or an Asx turn that resembles a Schellman loop) through hydrogen bonding of the side-chain carboxyl of Asp192 with the Met196 and Val197 backbone amides, and of the Asp192 backbone carbonyl with the backbone amide of Ser195. These consecutive turns also support a long-range hydrogen bond between the Asp187 backbone amide and the Pro193 carbonyl. These intramolecular interactions cooperate to form a well-defined structural element that makes multiple specific contacts with sKLB, burying a relatively large surface area of 606 Å^2.

Site 2 interactions with FGF21$_{CT}$ contrast markedly with site 1 interactions, and comprise a network of intermolecular interactions of the sort typically observed between proteins and short peptides (Fig. 2f and Extended Data Fig. 4a, b). Residues 200–209 of the FGF21$_{CT}$ peptide project into what would be the substrate-binding site occupied by glycosides that D2 of sKLB would hydrolyse if it were an active GH1 enzyme (Fig. 3 and see later). It is also noteworthy that half of the sequence of this part of FGF21$_{CT}$ (S-Q-G-R-S-P-S-Y-A-S) consists of residues with side-chain hydroxyl groups, suggesting that this region of FGF21 may indeed mimic a glycoside substrate. Given these characteristics, a notable feature of site 2 is the interaction between the side-chain carboxyl group of Glu693 in sKLB and hydroxyl groups of Ser204 and Ser206 in FGF21$_{CT}$ (Fig. 3d). Glu693 corresponds to one of the two conserved catalytic glutamates, and would function as a general acid–base catalyst in the Koshland double-displacement reaction of glycoside hydrolases; by contrast, in D2 the potential nucleophilic glutamate is replaced by alanine.

Amino acids 198–200 of FGF21$_{CT}$, which connect ligand-binding sites 1 and 2, do not make substantial contacts with sKLB. In addition, the electron densities in omit maps (Fig. 2b) and *B*-factors (Fig. 2c) suggest that this region is flexible. This conclusion is consistent with the previous identification of an enzyme that cleaves FGF21 in this region, and which is known to abolish the binding of FGF21 to β-klotho[10–15]. As this region of FGF21 is flexible and potentially accessible for proteolysis, cleavage between the binding regions of sites 1 and 2 could represent a mechanism for the termination of FGF21 signalling by targeted proteolysis.

The crystal structure of sKLB bound to FGF21$_{CT}$ reveals how the basic framework of a glycoside hydrolase has evolved to become a specific receptor for endocrine FGFs. The β-glucosidase family

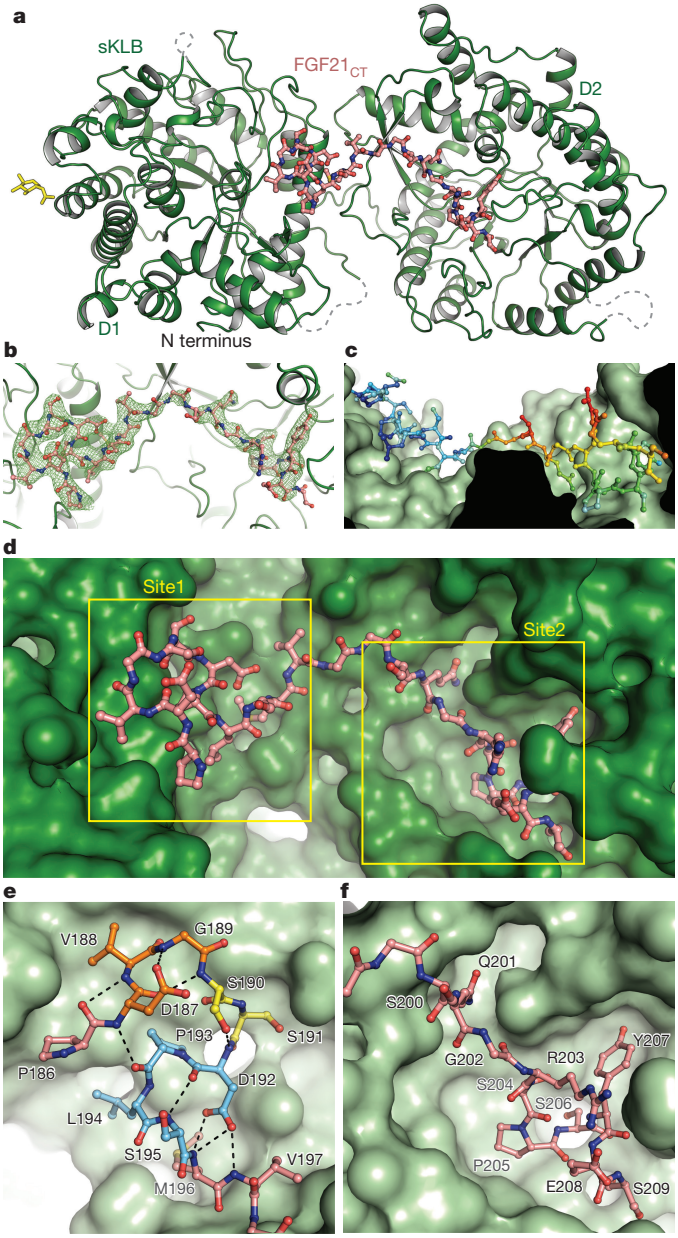

Figure 2 | Crystal structure of sKLB bound to $FGF21_{CT}$ reveals two distinct binding sites. a, The structure of sKLB (green) in complex with $FGF21_{CT}$ (salmon) is shown as a ribbon and ball-and-stick representation. Yellow sticks denote *N*-linked glycans. Nb914 is omitted for clarity. Grey dashed lines denote regions that do not exhibit significant electron densities. **b**, $FGF21_{CT}$ binding site showing $|F_o| - |F_c|$ omit map contoured at 3.0σ for $FGF21_{CT}$. **c**, Surface of sKLB interacting with $FGF21_{CT}$ are colour-coded according to *B*-factor values, which range from 52.76 $Å^2$ (blue) to 103.63 $Å^2$ (red). **d**, Surface representation of sKLB (green) highlighting two binding sites, site 1 and site 2 of $FGF21_{CT}$ (salmon, ball-and-stick). **e**, Site 1 forms a series of internal hydrogen bonds (black dashed lines) through three consecutive turns (orange, yellow and light blue), creating a structural element that binds to D1 of sKLB. **f**, Site 2 interacts with the pseudo-substrate-binding region of D2 of sKLB.

of glycoside hydrolases catalyse the hydrolysis of disaccharides as well as longer oligosaccharides, and several crystal structures of β-glucosidases in complex with oligosaccharide substrates such as cellotetraose (*Paenibacillus polymyxa* BglB, PDB code: 2Z1S) and cellopentaose (*Oryza sativa* BGlu1, PDB code: 3F5K) have previously been determined[16,17]. Superimposition of the crystal structures of substrate-bound β-glucosidases with the structure of sKLB in complex with $FGF21_{CT}$ shows that the backbone of residues 200–209 from $FGF21_{CT}$ aligns very well with the location of oligosaccharides that occupy the catalytic pocket of β-glucosidases (Fig. 3a–c). The mode of interaction between the hydroxyls of Ser204 and Ser206 from $FGF21_{CT}$ and the conserved glutamate in D2 of sKLB, together with hydrophobic interactions involving Pro205, are highly reminiscent of the substrate interactions seen for the glycoside hydrolases[6], suggesting that the sKLB—$FGF21_{CT}$ site 2 interaction is a pseudo-substrate interaction (Fig. 3d). Oligosaccharide substrates bound to the catalytic glutamic acid in the active sites of β-glucosidases lie in precisely the same position as the Ser204-Pro205-Ser206 motif of FGF21 bound to site 2 of sKLB. In addition, the residues in sKLB that form hydrophobic interactions with the Pro205 of FGF21—that is, Phe826, Phe931 and Phe942—align closely with the corresponding hydrophobic residues in β-glucosidases. These unexpected similarities indicate that the substrate-binding region of glycoside hydrolases evolved to recognize a sugar-mimicking Ser-Pro-Ser motif in FGF21 (Fig. 3e). As FGF19 also binds specifically to β-klotho, it is not surprising that FGF19 also contains a Ser211-Pro212-Ser213 motif at its C terminus (Extended Data Fig. 5), whereas FGF23—which does not bind to β-klotho—has no such sequence. Future studies that investigate how FGF23 recognizes α-klotho should provide guidance for the development of new treatments of metabolic disorders caused by impaired phosphate homeostasis[18], as well as information on the unique evolutionary pathway that this family of proteins may have taken.

We next analysed the binding affinities between sKLB and FGF21, the wild-type FGF21 C terminus or a range of mutations of the C-terminal tail of FGF21 to investigate the contributions of different amino acids in FGF21 that take part in the interface of the ligand-occupied sKLB structure. We also investigated the effects of mutations in the two $FGF21_{CT}$-binding sites of β-klotho on the ability of FGF21 to stimulate FGFR1 activation in transfected L6 rat myoblasts. These experiments validated the ligand-binding interfaces identified in the occupied sKLB structure and demonstrated that $FGF21_{CT}$ binds in a cooperative manner to both site 1 and site 2 in β-klotho (for full details of these experiments, see Extended Data Figs 6, 7 and Supplementary Discussion).

Because endocrine FGFs have important roles in the control of metabolic processes, a variety of approaches have previously been used to develop therapeutic variants of these proteins[12,19–24]. We reasoned that it should be possible to enhance the potency of FGF21, by introducing into its C-terminal tail mutations that strengthen interactions with β-klotho. We introduced a Leu194Phe mutation to increase hydrophobic interactions with neighbouring amino acids in site 1 of β-klotho, and an Arg203Trp mutation to replace cation–π interactions between Arg203 in FGF21 and His646 in site 2 of β-klotho with π–π interactions. We found that FGF21 with the Arg203Trp and Leu194Phe substitutions ($FGF21_{WF}$) bound to sKLB over tenfold more tightly than wild-type FGF21, with a dissociation constant (K_d) value of 3.4 ± 1.2 nM (Fig. 4a), and that the $FGF21_{WF}$ mutant had an enhanced ability to stimulate FGFR1c autophosphorylation and MAP kinase stimulation in L6 cells that co-express β-klotho and FGFR1c (Fig. 4b and Extended Data Fig. 8).

These experiments show that, rather than serving as an alternative co-receptor for FGFR1c activation by endocrine FGFs, β-klotho functions as the primary high-affinity receptor for FGF21. We show that klotho proteins function as specific zip-code-like signals for targeting FGF21 (or two other endocrine FGFs) to cells and tissues, where they mediate their cellular responses by activating members of the FGFR families. The scheme presented in Fig. 4c depicts a model of how FGF21 binding to β-klotho enables it to activate a β-klotho–FGFR complex to promote cell signalling. In the model, FGFR1c and β-klotho monomers exist in equilibrium with β-klotho–FGFR heterodimers in the membrane. With a K_d value of approximately 1 μM for the binding of the FGFR1c extracellular region to sKLB (Extended Data Fig. 6b), a substantial portion of FGFR1c and β-klotho will be associated with one another at levels of around 10,000 copies per cell. FGF21 binds

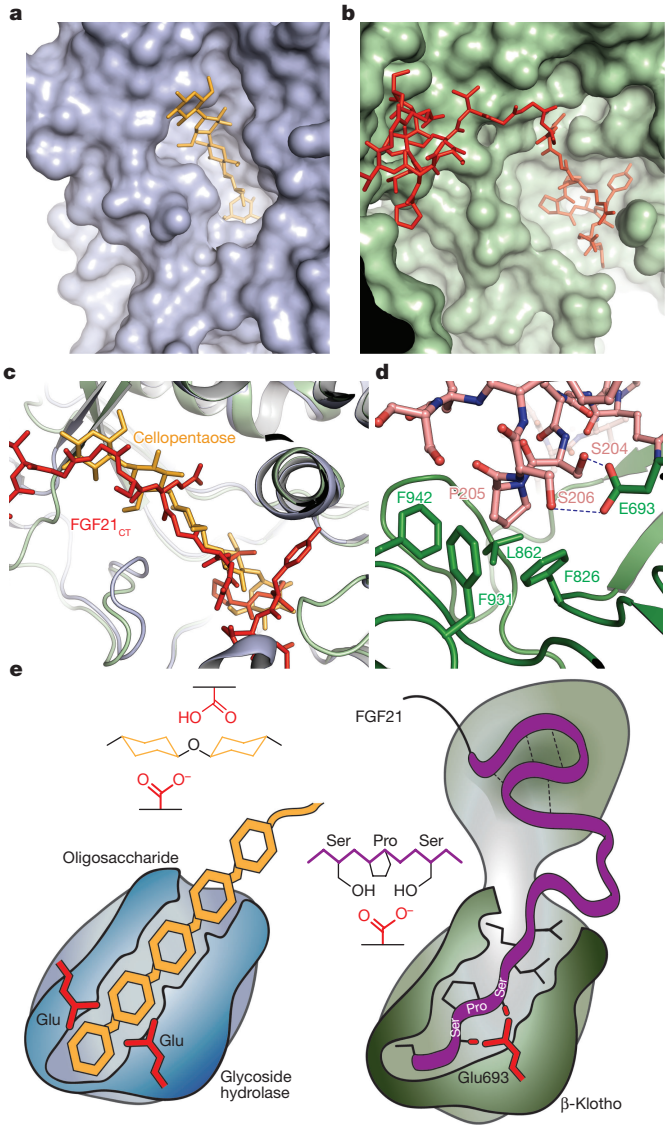

Figure 3 | Comparison of β-glucosidase and β-klotho structures and the evolution of a sugar-cutting enzyme into a receptor for endocrine FGF. a, **b**, The structure of rice β-glucosidase (**a**) (light blue, surface representation) in complex with cellopentaose (orange, stick representation) (PDB code: 3F5K) and site 2 of sKLB (**b**) (pale green, surface representation) in complex with $FGF21_{CT}$ (red, stick representation). Cellopentaose binds to the active site of β-glucosidase and $FGF21_{CT}$ binds to the corresponding pseudo-substrate binding site of β-klotho. **c**, Superimposition of the structures of cellopentaose-bound rice β-glucosidase and $FGF21_{CT}$-bound sKLB. **d**, Glu693 of β-klotho makes contacts with Ser-Pro-Ser motif of FGF21 via interaction with the hydroxyl moieties of serine residues, mimicking the sugar hydroxyls in their interaction with glutamate residues in the catalytic site of β-glucosidase. **e**, Schematic diagram comparing the substrate-binding pocket including the two glutamic acid residues required for glycoside hydrolase activity with the ligand-binding pocket of β-klotho depicting interactions between Glu693 and the Ser-Pro-Ser motif.

with high affinity (K_d = 43.5 nM, Extended Data Fig. 6a) either to β-klotho monomers or to pre-existing β-klotho–FGFR1c heterodimers. With FGF21 thus tethered via its C-terminal tail to β-klotho monomers and/or β-klotho–FGFR1c heterodimers, all three components are reduced to two dimensions at the membrane and the weak—but demonstrable—affinity of the FGF core of FGF21 for FGFR1c is sufficient to drive the formation of the activated ternary FGF21–FGFR1c–β-klotho complex via a reduced dimensionality effect on the bivalent binding of FGF to two FGFR molecules[25]. In this model, β-klotho

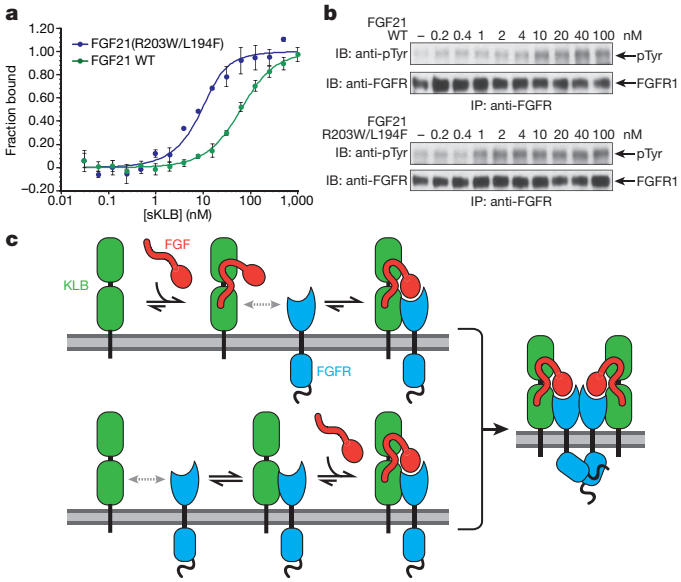

Figure 4 | Structure-based engineering of an FGF21 analogue with enhanced biological activity and the mechanism of endocrine FGF signalling. a, **b**, Enhanced binding affinity (**a**) and bioactivity (**b**) of an FGF21 mutant. Microscale thermophoresis (MST) binding measurements of FGF21 with Leu194Phe and Arg203Trp mutations in the C-terminal tail reveal an approximately tenfold increase in binding affinity to sKLB, with a K_d value of 3.4 ± 1.3 nM, and an approximately tenfold enhanced potency for stimulation of FGFR1c tyrosine phosphorylation. The dots and error bars in **a** denote mean and s.d. of ΔF_{norm} (n = 3 independent samples). Individual experimental data are plotted in Extended Data Fig. 9. **c**, A zip-code-like mechanism for β-klotho-dependent FGF21 stimulation of FGFR1c. In the cell membrane of unstimulated cells, β-klotho and FGFR1c monomers are in equilibrium with β-klotho–FGFR heterodimers. Owing to reduced dimensionality, the binding of FGF21 to β-klotho via the FGF21 C-terminal tail, and the bivalent binding of the FGF core of FGF21 to two FGFR1c molecules, will shift the equilibrium towards the formation of an FGF21–FGFR1c–β-klotho ternary complex, and result in the stimulation of tyrosine kinase activity and cell signalling via FGFR1c. In addition, β-klotho functions as a primary high-affinity receptor for FGF21, and FGFR1c functions as a catalytic subunit that mediates receptor dimerization and intracellular signalling.

functions as a primary high-affinity receptor for FGF21, whereas FGFR1c functions as a catalytic subunit that mediates receptor dimerization and intracellular signalling.

The crystal structure of sKLB bound to $FGF21_{CT}$ also provides clear evidence for how the two glycoside hydrolase-like domains of β-klotho have been 'repurposed' in evolution to recognize FGF21 specifically. By comparing the structures of substrate-bound β-glucosidases to the second glycoside hydrolase-like domain of $FGF21_{CT}$-bound β-klotho, we reveal how the active site of an enzyme specialized for cutting sugars has evolved to become a specific and high-affinity cell-surface receptor for circulating hormones that regulate essential metabolic processes including the lowering of blood sugar levels—this may not be a coincidence. The structure of the C terminus of FGF21 appears to mimic that of an oligosaccharide. The similarities between FGF21 and FGF19 indicate that the specificity of these two hormones towards β-klotho, and their modes of action, are very similar (Extended Data Fig. 5). Differences in the cellular responses to these two endocrine FGFs are likely to be determined by the altered binding preferences of the two ligands for the different FGFRs.

Online Content Methods, along with any additional Extended Data display items and Source Data, are available in the online version of the paper; references unique to these sections appear only in the online paper.

Received 11 July; accepted 3 November 2017.
Published online 17 January 2017.

1. Eswarakumar, V. P., Lax, I. & Schlessinger, J. Cellular signaling by fibroblast growth factor receptors. *Cytokine Growth Factor Rev.* **16,** 139–149 (2005).
2. Belov, A. A. & Mohammadi, M. Molecular mechanisms of fibroblast growth factor signaling in physiology and pathology. *Cold Spring Harb. Perspect. Biol.* **5,** a015958 (2013).
3. Ogawa, Y. *et al.* βKlotho is required for metabolic activity of fibroblast growth factor 21. *Proc. Natl Acad. Sci. USA* **104,** 7432–7437 (2007).
4. Urakawa, I. *et al.* Klotho converts canonical FGF receptor into a specific receptor for FGF23. *Nature* **444,** 770–774 (2006).
5. Owen, B. M., Mangelsdorf, D. J. & Kliewer, S. A. Tissue-specific actions of the metabolic hormones FGF15/19 and FGF21. *Trends Endocrinol. Metab.* **26,** 22–29 (2015).
6. Koshland, D. E. Jr. Stereochemistry and the mechanism of enzymatic reactions. *Biol. Rev. Camb. Philos. Soc.* **28,** 416–436 (1953).
7. Holm, L. & Rosenström, P. Dali server: conservation mapping in 3D. *Nucleic Acids Res.* **38,** W545–W549 (2010).
8. Krissinel, E. & Henrick, K. Inference of macromolecular assemblies from crystalline state. *J. Mol. Biol.* **372,** 774–797 (2007).
9. Hayward, S. & Lee, R. A. Improvements in the analysis of domain motions in proteins from conformational change: DynDom version 1.50. *J. Mol. Graph. Model.* **21,** 181–183 (2002).
10. Yie, J. *et al.* FGF21 N- and C-termini play different roles in receptor interaction and activation. *FEBS Lett.* **583,** 19–24 (2009).
11. Micanovic, R. *et al.* Different roles of N- and C- termini in the functional activity of FGF21. *J. Cell. Physiol.* **219,** 227–234 (2009).
12. Hecht, R. *et al.* Rationale-based engineering of a potent long-acting FGF21 analog for the treatment of type 2 diabetes. *PLoS ONE* **7,** e49345 (2012).
13. Zhen, E. Y., Jin, Z., Ackermann, B. L., Thomas, M. K. & Gutierrez, J. A. Circulating FGF21 proteolytic processing mediated by fibroblast activation protein. *Biochem. J.* **473,** 605–614 (2016).
14. Dunshee, D. R. *et al.* Fibroblast activation protein cleaves and inactivates fibroblast growth factor 21. *J. Biol. Chem.* **291,** 5986–5996 (2016).
15. Coppage, A. L. *et al.* Human FGF-21 is a substrate of fibroblast activation protein. *PLoS ONE* **11,** e0151269 (2016).
16. Chuenchor, W. *et al.* The structural basis of oligosaccharide binding by rice BGlu1 beta-glucosidase. *J. Struct. Biol.* **173,** 169–179 (2011).
17. Isorna, P. *et al.* Crystal structures of *Paenibacillus polymyxa* β-glucosidase B complexes reveal the molecular basis of substrate specificity and give new insights into the catalytic machinery of family I glycosidases. *J. Mol. Biol.* **371,** 1204–1218 (2007).
18. Degirolamo, C., Sabbà, C. & Moschetta, A. Therapeutic potential of the endocrine fibroblast growth factors FGF19, FGF21 and FGF23. *Nat. Rev. Drug Discov.* **15,** 51–69 (2016).
19. Kharitonenkov, A. *et al.* Rational design of a fibroblast growth factor 21-based clinical candidate, LY2405319. *PLoS ONE* **8,** e58575 (2013).
20. Huang, Z. *et al.* A better anti-diabetic recombinant human fibroblast growth factor 21 (rhFGF21) modified with polyethylene glycol. *PLoS ONE* **6,** e20669 (2011).
21. Huang, J. *et al.* Development of a novel long-acting antidiabetic FGF21 mimetic by targeted conjugation to a scaffold antibody. *J. Pharmacol. Exp. Ther.* **346,** 270–280 (2013).
22. Foltz, I. N. *et al.* Treating diabetes and obesity with an FGF21-mimetic antibody activating the βKlotho/FGFR1c receptor complex. *Sci. Transl. Med.* **4,** 162ra153 (2012).
23. Luo, J. *et al.* A nontumorigenic variant of FGF19 treats cholestatic liver diseases. *Sci. Transl. Med.* **6,** 247ra100 (2014).
24. Kolumam, G. *et al.* Sustained brown fat stimulation and insulin sensitization by a humanized bispecific antibody agonist for fibroblast growth factor receptor 1/βklotho complex. *EBioMedicine* **2,** 730–743 (2015).
25. Schlessinger, J. *et al.* Crystal structure of a ternary FGF–FGFR–heparin complex reveals a dual role for heparin in FGFR binding and dimerization. *Mol. Cell* **6,** 743–750 (2000).

Supplementary Information is available in the online version of the paper.

Acknowledgements The NSLS-SSRL is supported by P41GM111244, P41GM103393, DE-SC0012704 and by DE-AC02-76SF00515. We thank NE-CAT (P41 GM103403) and APS (DE-AC02-06CH11357). This research was also supported by NIH grant 1S10OD018007 and NIH Award S10RR026992-0110. J.St. thanks INSTRUCT (ESFRI, FWO) for financial support and I. Aboutaleb for technical assistance.

Author Contributions S.L. designed, performed experiments and determined the crystal structures. J.C., J.M. and F.T. provided technical support. E.P. and J.St. generated nanobodies. L.P.S. and I.L. designed and analysed cell-based experiments. S.L., M.A.L. and J.Sc. designed experiments, analysed data and wrote the manuscript.

Author Information Reprints and permissions information is available at www.nature.com/reprints. The authors declare no competing financial interests. Readers are welcome to comment on the online version of the paper. Publisher's note: Springer Nature remains neutral with regard to jurisdictional claims in published maps and institutional affiliations. Correspondence and requests for materials should be addressed to J.Sc. (joseph.schlessinger@yale.edu).

Reviewer Information *Nature* thanks N. Jura, K. White, H. E. Xu and the other anonymous reviewer(s) for their contribution to the peer review of this work.

METHODS

Plasmid construction. cDNAs that encode for either amino acids 30–983 (sKLB) or 30–522 (KLB_{D1}) of human β-klotho (KLB) were amplified together with the tobacco etch virus (TEV) protease cleavage site and linker of four Gly residues. The resulting sequence was subcloned into a modified pCEP4 vector (Thermo Fisher Scientific) that contains the sequence for the Fc region of human IgG1. The expression vector for C-terminal HA-tagged KLB was generated by subcloning the gene of full-length KLB together with the haemagglutinin (HA)-tag sequence into a pBABE vector. All plasmids of KLB mutants were generated by following standard site-directed mutagenesis protocol using a plasmid containing wild-type C-terminal HA-tagged KLB.

Expression and purification of sKLB and KLB_{D1}. HEK293 EBNA cells were cultured in a humidified incubator with 5% CO_2 at 37 °C in DMEM (Thermo Fisher Scientific) containing 10% fetal bovine serum (FBS), 100 U ml^{-1} penicillin–streptomycin, and 250 μg ml^{-1} G418. The plasmids were transfected into HEK293 EBNA cells with the Lipofectamine 2000 (Thermo Fisher Scientific) and selected by treatment with 200 μg ml^{-1} of hygromycin B (Thermo Fisher Scientific) for 2–3 weeks. Cells stably expressing sKLB–Fc or KLB_{D1}–Fc were expanded in Hyperflasks (Corning), and the medium was changed to DMEM with 5% FBS when cell confluency had reached about 70%. After 7 days, the medium was collected after centrifugation at 5,000*g* and filtration through a 0.2-μm membrane. Swainsonine (15 μM; Cayman Chemical) was added to the medium of cultured cells when preparing proteins for crystallization.

Medium collected from the cells expressing sKLB–Fc or KLB_{D1}–Fc was incubated with recombinant protein A sepharose 4B (Thermo Fisher Scientific) overnight at 4 °C. The resin was washed with 50 column volumes of PBS and the protein was eluted from the resin using 0.1 M glycine–HCl, pH 3.5, and immediately neutralized with 0.1 M Tris, pH 7.4. The eluted protein was incubated with recombinant TEV protease for 2 h at room temperature to cleave the C-terminal Fc tag, followed by incubation with recombinant protein A sepharose 4B for 30 min at 4 °C to remove Fc tag and undigested protein. The protein was then subjected to cation exchange chromatography (Mono S 5/50 GL, GE Healthcare) using 20 mM sodium phosphate buffer at pH 7.0 (for sKLB) or at pH 6.5 (for KLB_{D1}), and purified using a linear salt gradient. The elution fractions containing sKLB or KLB_{D1} were pooled, concentrated and subjected to a Superdex 200 Increase 10/300 GL (GE Healthcare) size-exclusion chromatography column pre-equilibrated with 20 mM HEPES, 150 mM NaCl, pH 7.0. The eluted fractions containing sKLB or KLB_{D1} were pooled, concentrated, flash-frozen and stored at −80 °C until further use. For the crystallization of sKLB, two potential *N*-glycosylation sites, Asn308 and Asn611, were mutated to glutamine. The mutations were introduced to the sKLB–Fc plasmid by standard QuikChange site-directed mutagenesis. The expression and purification of mutant sKLB was identical to that used for wild-type sKLB. The typical yield of sKLB after complete purification was 1–2 mg per litre of medium from the cells that stably expressed sKLB.

Expression and purification of recombinant FGF21, GST–$FGF21_{CT}$ and $FGFR1c_{D2D3}$. The DNA sequence that encodes for human FGF21 amino acids 29–209 with three mutations—Leu126Arg, Pro199Gly and Asn208Glu—was codon-optimized for *Escherichia coli* expression and synthesized (Blue Heron Biotech). After cloning into a pET28a vector (Novagen), the plasmid was transformed into BL21-Gold (DE3) competent cells. Transformants were grown in LB medium containing 50 μg ml^{-1} kanamycin, shaken at 240 r.p.m. at 37 °C. When the $A_{600\,nm}$ of the samples reached 0.6, the bacteria were induced with 1 mM IPTG for 4 h at 37 °C. The bacterial cell pellet, collected by centrifugation at 5,000*g* at 4 °C, was lysed in 20 mM sodium phosphate buffer, 500 mM NaCl, 5% glycerol, pH 7.8, using EmulsiFlex-C3 homogenizer (Avestin), followed by centrifugation at 20,000*g* for 30 min at 4 °C. The supernatant containing N-terminal His_6-tagged FGF21 was supplemented with 10 mM imidazole and incubated with Ni-NTA agarose (Qiagen) for 1 h at 4 °C. The resin was washed with a 20 column volume of lysis buffer containing 10 mM imidazole, and the protein was eluted from the resin with lysis buffer containing 300 mM imidazole. The protein solution was injected into a HiLoad 26/600 Superdex 200 (GE Healthcare) size-exclusion chromatography column equilibrated with 20 mM HEPES, 900 mM NaCl at pH 7.5. The eluted fractions containing FGF21 were pooled, concentrated to about 1.5 mg ml^{-1}, flash-frozen and stored at −80 °C. To generate glutathione *S*-transferase (GST)-tagged $FGF21_{CT}$, a DNA sequence encoding amino acids 169–209 of FGF21 was cloned into pGEX-4T-1 vector (GE Healthcare), and the plasmid was transformed into BL21-Gold (DE3) competent cells (Agilent). Transformants were grown in LB medium containing 100 μg ml^{-1} ampicillin at 37 °C until $A_{600\,nm}$ reached 0.6, and induced with 1 mM IPTG for 4 h at 37 °C. Bacteria cells were collected, lysed in PBS using EmulsiFlex-C3 homogenizer (Avestin), and centrifuged at 20,000*g* for 30 min at 4 °C. The supernatant containing GST–$FGF21_{CT}$ was incubated with glutathione sepharose 4B (GE Healthcare) pre-equilibrated with PBS, for 1 h at 4 °C. The beads were washed with 50 column volumes of PBS and the protein was eluted with 20 mM HEPES, 150 mM NaCl, 10 mM reduced glutathione, pH 7.3. The protein solution containing GST–$FGF21_{CT}$ was then dialysed against 20 mM HEPES, 150 mM NaCl before flash-freezing and storage at −80 °C. A peptide corresponding to the C-terminal region of FGF21 containing amino acids 174–209 with two substitutions, Pro199Gly and Ala208Glu, was synthesized and purified by the Tufts University Core Facility. The ligand-binding region of FGFR1c was expressed in *E. coli* as an insoluble fraction. The protein was refolded and purified as previously described[25].

Expression and purification of Nb914. The plasmid containing C-terminal His_6-tagged Nb914 was transformed into *E. coli* strain WK6, and grown in TB medium containing 0.1% glucose, 2 mM $MgCl_2$, and 100 μg ml^{-1} ampicillin at 37 °C until the $A_{600\,nm}$ of the sample was 1.2, and then induced with 1 mM IPTG for 4 h. Cells were collected and the periplasmic fraction was extracted using the modified osmotic shock protocol[26]. The periplasmic extract containing Nb914 was supplemented with 10 mM imidazole and incubated with Ni-NTA agarose (Qiagen) for 1 h at 4 °C. The beads were washed with 50 column volumes of PBS containing 10 mM imidazole, and Nb914 was eluted from the resin with PBS containing 300 mM imidazole. The eluted fraction containing Nb914 were concentrated and injected into a HiLoad 26/600 Superdex 200 (GE Healthcare) size-exclusion chromatography column pre-equilibrated with PBS at pH 7.0. Purified Nb914 at a concentration of 10 mg ml^{-1} was flash-frozen and stored at −80 °C.

Crystallization, X-ray diffraction data collection and structure determination. Purified sKLB or KLB_{D1} was mixed with Nb914, concentrated and injected into a Superdex 200 Increase 10/300 GL (GE Healthcare) size-exclusion chromatography column pre-equilibrated with 20 mM HEPES, 150 mM NaCl, pH 7.0. Eluted fractions containing the complex were pooled, concentrated to 7 mg ml^{-1} and screened for crystallization using Mosquito Crystal liquid handler (TTP Labtech). Ninety-six-well plates were incubated and imaged at 20 °C using Rock Imager 1000 (Formulatrix). sKLB in complex with Nb914 produced rod-shaped crystals when mixed with an equal volume of well solution containing 14% PEG4000, 0.1 M MES, pH 6.0 and equilibrated for 10–15 days using the hanging-drop vapour diffusion method. The crystals were cryopreserved by gradually transferring crystals to the mother liquor supplemented with 30% glucose before being flash-frozen in liquid nitrogen. KLB_{D1} in complex with Nb914 gave plate-like crystals when mixed with an equal volume of well solution containing 30% PEG1000, 0.1 M HEPES pH 7.5 and equilibrated for 4–6 days using the hanging-drop vapour diffusion method; these crystals were directly flash-frozen in liquid nitrogen. For sKLB in complex with Nb914 and $FGF21_{CT}$, $FGF21_{CT}$ was dissolved in 14% PEG4000, 0.1 M MES, pH 6.0 and added to the drop containing crystals of sKLB. The addition of $FGF21_{CT}$ immediately caused deformation in most of the crystals. Crystals that stayed intact were gradually transferred into the artificial mother liquor, supplemented with 30% glucose and 50 μM $FGF21_{CT}$, before being flash-frozen in liquid nitrogen. X-ray diffraction data were collected at the beamline BL-14 at the Stanford Synchrotron Radiation Lightsource, SLAC National Accelerator Laboratory (for KLB_{D1} and sKLB) and 24-ID-E at the Advanced Photon Source, Argonne (for sKLB in complex with $FGF21_{CT}$). The diffraction datasets were processed using HKL2000[27] and XDS[28]. Initial phases for the dataset for KLB_{D1} in complex with Nb914 were calculated by molecular replacement with PHASER[29] using the coordinates of the cytosolic β-glucosidase (PDB code: 2ZOX) and the coordinates of a nanobody that exhibits the highest sequence identities with Nb914 (PDB code: 5IMK, chain B) as the search models. Refinement was iteratively performed using PHENIX[30] followed by manual model building using Coot[31]. The final coordinates of KLB_{D1} in complex with Nb914 were then used as a search model for the dataset of sKLB in complex with Nb914, together with the coordinates for KLB_{D1}, as a search model for D2 of sKLB. Then, the model was iteratively built and refined for sKLB. For the dataset for sKLB in complex with Nb914 and $FGF21_{CT}$, initial phase information was obtained by molecular replacement using the final coordinates of sKLB in complex with Nb914, which were divided into two models each containing the coordinates for D1 with Nb914 and D2, and searched independently. Iterative cycles of refinement and rebuilding of the sKLB model improved the phase, and produced significant electron densities for $FGF21_{CT}$. Subsequently, the model for $FGF21_{CT}$ was manually built on the basis of the $|F_o| - |F_c|$ map, followed by the final refinement cycles. The data collection and refinement statistics are summarized in Supplementary Table 1. All the figures containing the structures were generated using the PyMOL Molecular Graphics System, version 1.8 (Schrödinger).

MST measurements. All MST measurements were performed using the Monolith NT.115Pico instrument (NanoTemper) with Monolith NT.115 MST Premium Coated Capillaries. Purified FGF21 was fluorescently labelled using the Monolith Protein Labelling Kit RED-NHS (NanoTemper) according to the manufacturer's instructions. Samples for binding-affinity measurements of FGF21 to sKLB were prepared by mixing 35 nM of fluorescently labelled FGF21 (fl-FGF21) with a series of concentrations (0.03–1,000 nM) of purified sKLB in 20 mM HEPES, 150 mM NaCl, pH 7.0, 0.05% Tween-20, 1 mg ml^{-1} BSA. The thermophoretic movements

of fl-FGF21 in each sample were monitored (LED 20%, IR laser 20%) and the normalized fluorescence intensities (F_{norm}), defined as F_{hot}/F_{cold} (where F_{cold} and F_{hot} refer to the fluorescence intensities averaged over a 1-s period before the IR laser was turned on and 29 s after IR laser was turned on, respectively) for each sample were plotted against the concentrations of sKLB. For the competition assays, the thermophoresis of fl-FGF21 was measured for samples in which the concentration of fl-FGF21 and sKLB mixture was kept constant, with concentrations of GST–$FGF21_{CT}$ varying from 2.1 nM to 35,000 nM. All the data were analysed with the MO.Affinity Analysis software (NanoTemper) provided by the manufacturer.

Surface plasmon resonance measurements. All surface plasmon resonance experiments were performed using a BIAcore T100 instrument (GE Healthcare) at 25 °C (Keck Foundation Biotechnology Resource Laboratory) using HPBS + buffer (GE Healthcare). Anti-GST antibody (GE Healthcare) was immobilized on a CM5 sensor chip using the instructions provided, followed by capturing 50 response units (RU) of GST–$FGF21_{CT}$. Using the single-cycle kinetics method, a series concentration of sKLB ranging from 25.6 nM to 1,000 nM was subsequently injected onto the surfaces with 360 s of association period, followed by the dissociation period of 1,200 s. The binding kinetics were evaluated using BIAevaluation software (GE Healthcare).

Cell-based activity assays. L6 cells that stably co-expressed wild-type FGFR1c, together with either wild-type β-klotho or a variety of β-klotho mutants, were grown in DMEM supplemented with 10% FBS, 100 U ml^{-1}, penicillin–streptomycin, 0.1 mg ml^{-1} hygromycin and 1 μg ml^{-1} puromycin. Cells were starved overnight in DMEM with 0.5% FBS and stimulated for 10 min at 37 °C with either FGF1 or FGF21 at concentrations of 5 nM and 25 nM, respectively. Cells were then lysed and subjected to immunoprecipitation with anti-FGFR1 antibody, followed by SDS–PAGE. The samples were then subjected to immunoblotting with anti-phosphotyrosine (pTyr), anti-β-klotho or anti-FGFR1 antibodies.

Statistics and reproducibility. No statistical methods were used to predetermine sample size. All of the immunoblots and binding affinity measurements presented in this work were repeated at least three times with similar results.

Data availability. Coordinates and structure factors for the complexes have been deposited in the Protein Data Bank (PDB) under accessions 5VAK (KLB_{D1}–Nb914), 5VAN (sKLB–Nb914) and 5VAQ (sKLB–$FGF21_{CT}$–Nb914). All other data are available from the corresponding author upon reasonable request.

26. Pardon, E. *et al.* A general protocol for the generation of nanobodies for structural biology. *Nat. Protoc.* **9,** 674–693 (2014).
27. Otwinowski, Z. & Minor, W. Processing of X-ray diffraction data collected in oscillation mode. *Methods Enzymol.* **276,** 307–326 (1997).
28. Kabsch, W. Xds. *Acta Crystallogr. D* **66,** 125–132 (2010).
29. McCoy, A. J. *et al.* Phaser crystallographic software. *J. Appl. Crystallogr.* **40,** 658–674 (2007).
30. Adams, P. D. *et al.* PHENIX: a comprehensive Python-based system for macromolecular structure solution. *Acta Crystallogr. D* **66,** 213–221 (2010).
31. Emsley, P., Lohkamp, B., Scott, W. G. & Cowtan, K. Features and development of Coot. *Acta Crystallogr. D* **66,** 486–501 (2010).
32. Laskowski, R. A. & Swindells, M. B. LigPlot+: multiple ligand–protein interaction diagrams for drug discovery. *J. Chem. Inf. Model.* **51,** 2778–2786 (2011).

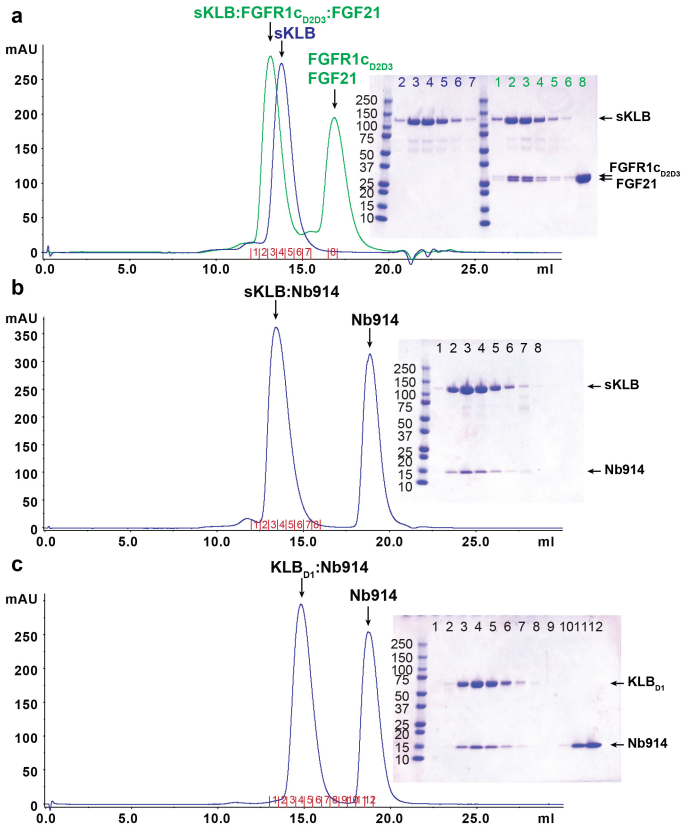

Extended Data Figure 1 | Expression, purification and crystallization of β-klotho extracellular domain. a–c, Size-exclusion chromatography profiles and corresponding Coomassie-stained SDS–PAGE gels of the sKLB–FGFR1c$_{D2D3}$–FGF21 ternary complex (green) or sKLB alone (blue) (**a**), sKLB in complex with Nb914 (**b**) and KLB$_{D1}$ in complex with Nb914 (**c**). The chromatograms and the SDS–PAGE gels shown are representatives of at least three independent preparations with similar results. A secreted protein composed of the extracellular domain of KLB fused to the Fc region of human IgG1 was produced by HEK293 EBNA cells. Following purification using a protein A agarose resin, the KLB–Fc fusion protein was subjected to proteolytic cleavage. sKLB was further purified using ion exchange and size-exclusion chromatography. Multiple crystallization trials with the ternary complex formed by sKLB, FGF21 and FGFR1c$_{D2D3}$ (**a**, green) failed to yield diffraction-quality crystals. However, a preparation of sKLB bound to a nanobody Nb914 (**b**) yielded crystals that diffracted X-rays to a resolution of 6–8 Å, and these were further improved by mutating two of the eleven potential *N*-glycosylation sites in sKLB (Asn308 and Asn611) to glutamine residues. The resulting crystals of an sKLB–Nb914 complex diffracted to a resolution of 2.2 Å. We also crystallized KLB$_{D1}$ in complex with Nb914 (**c**), and collected data to a resolution of 1.7 Å. The structure of KLB$_{D1}$ was first solved by molecular replacement using the coordinates of a structure of human cytosolic β-glucosidase (PDB code: 2ZOX) and the coordinates of a nanobody structure (PDB code: 5IMK, chain B) as search models. The structure of sKLB was subsequently determined by molecular replacement using the KLB$_{D1}$ coordinates as a search model.

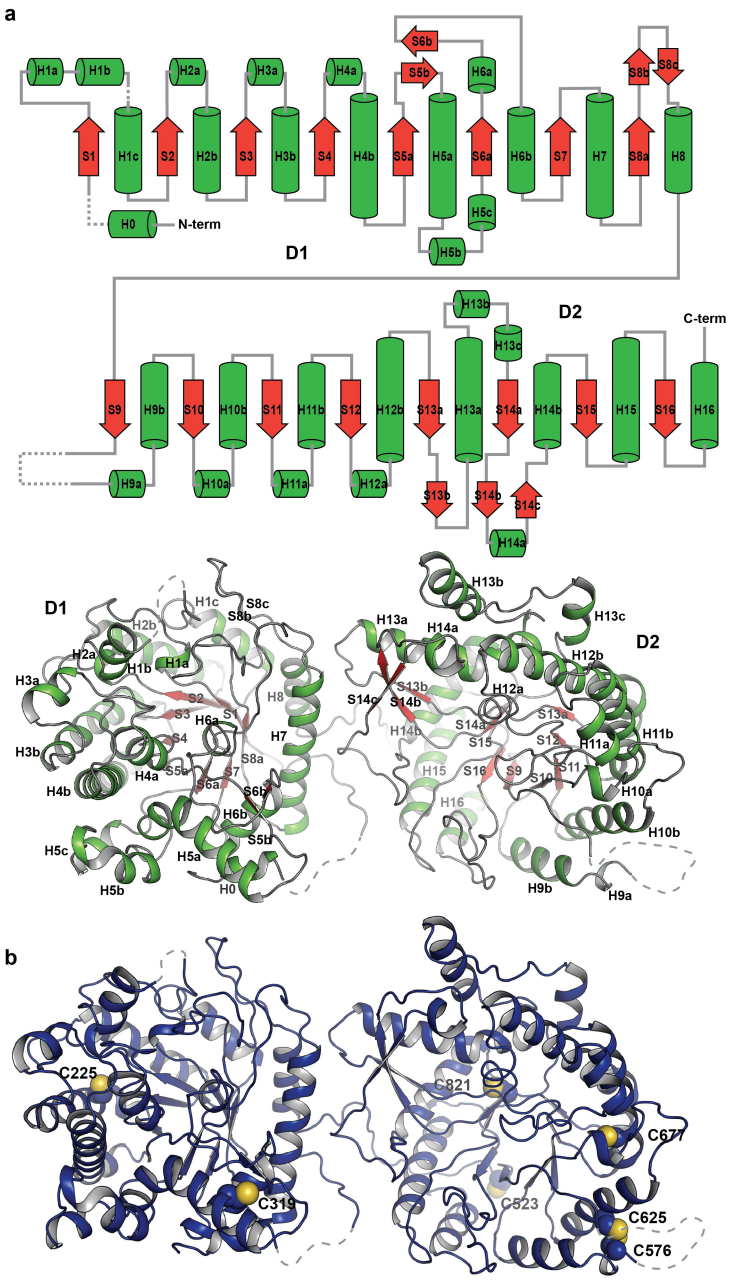

Extended Data Figure 2 | Domain diagram of sKLB structure and the location of cysteine residues. a, Secondary structure elements (H for helix (green) and S for sheet (red)) are designated by numbers on the basis of the principal elements for the $(\beta/\alpha)_8$ fold. Dashed lines depict disordered loops that are not modelled in the structure. **b**, Seven of the ten cysteine residues in the extracellular region were successfully modelled in the sKLB structure. With the exception of the disulfide bond between Cys576 and Cys625, the structure shows that these cysteine residues are reduced and do not form disulfide bridges. Moreover, determination of the distances between each pair of cysteines indicates that most are too far apart to form intramolecular disulfide bonds. However, we cannot rule out the possibility that Cys976 located in the C-terminal region of sKLB, which could not be modelled owing to weak electron density, may form a disulfide bond with the nearby Cys523. There is no evidence for the formation of intermolecular disulfide bonds between β-klotho and the closely associated FGFR, FGF19 or FGF21 proteins, whose cysteines all form well-characterized intramolecular disulfide bonds. The functional consequences of the presence of reduced cysteines in β-klotho are currently unknown.

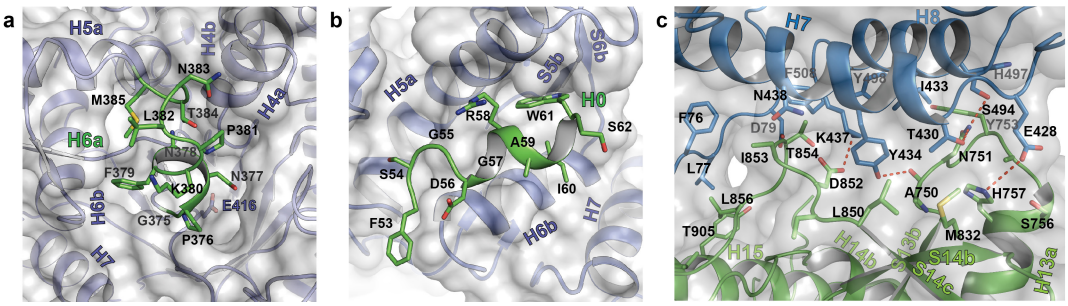

Extended Data Figure 3 | Unique structural features of sKLB. **a**, Interaction of H6a (green) with the pseudo-substrate binding pocket in D1 of sKLB. Glu416, the pseudo-catalytic glutamic acid residue in D1, is located on the bottom of the pocket and is also highlighted. **b**, Interaction of H0 (green) with the nearby structural elements in D1 of sKLB. **c**, Interface between D1 (blue) and D2 (green) of sKLB, highlighting amino acids and structural elements as well as polar interactions (red dotted lines) between the domains.

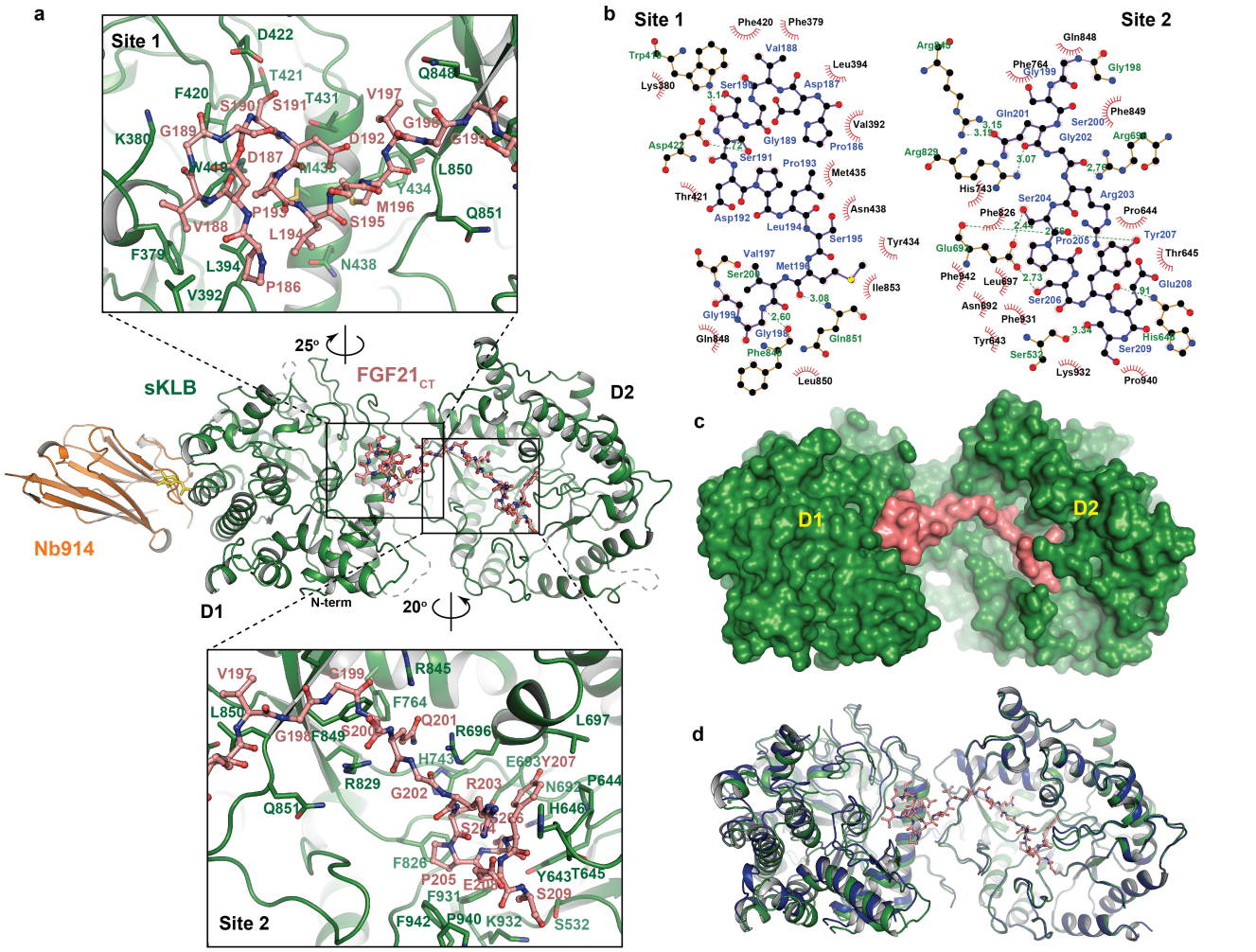

Extended Data Figure 4 | Details of interactions between sKLB and FGF21$_{CT}$, and conformational changes upon ligand binding. **a**, Interactions between amino acid residues in sKLB (green) and FGF21$_{CT}$ (salmon) in the areas of sites 1 and 2 are indicated. **b**, Diagram of amino-acid-specific interactions between sKLB and FGF21$_{CT}$ within sites 1 and 2. The figure was generated using Ligplot+[32]. **c**, Structure of sKLB (green) in complex with FGF21$_{CT}$ (salmon) shown as a surface representation. **d**, Structure of ligand-free sKLB (blue) is overlaid onto the structure of sKLB (green) bound to FGF21$_{CT}$ (salmon, ball-and-stick).

Extended Data Figure 5 | Amino acid sequence alignments of C-terminal regions of human FGF19 and FGF21. Residues Asp-Pro, which are critical in maintaining multi-turn elements, are highlighted in blue, and the sugar-mimicking motif Ser-Pro-Ser is highlighted in yellow. The sequence alignment reveals close sequence similarity between the C-terminal tails of FGF21 and FGF19 that is consistent with the similar binding characteristics of FGF21 and FGF19 and their isolated C-terminal regions to β-klotho. The sugar-mimicking motif in FGF21, Ser205-Pro206-Ser207, is conserved in FGF19 (Ser211-Pro212-Ser213). The sequence Asp192-Pro193, in the region of $FGF21_{CT}$ that binds to site 1 of β-klotho by stabilizing intramolecular hydrogen bonds that maintain a turn in the bound configuration of $FGF21_{CT}$, is also highlighted. This sequence is conserved in FGF19 (Asp198-Pro199), which suggests that intramolecular interactions similar to those responsible for mediating consecutive turns in $FGF19_{CT}$ may also bind to site-1 of β-klotho. Because many of the intramolecular interactions within $FGF21_{CT}$ bound to β-klotho take place between main-chain atoms (as observed in typical β-turn structures), the presence of only a few key amino acid sequences such as Asp198-Pro199 may be sufficient to generate multi-turn elements in $FGF19_{CT}$ that are similar to those observed in the crystal structure of $FGF21_{CT}$ bound to β-klotho.

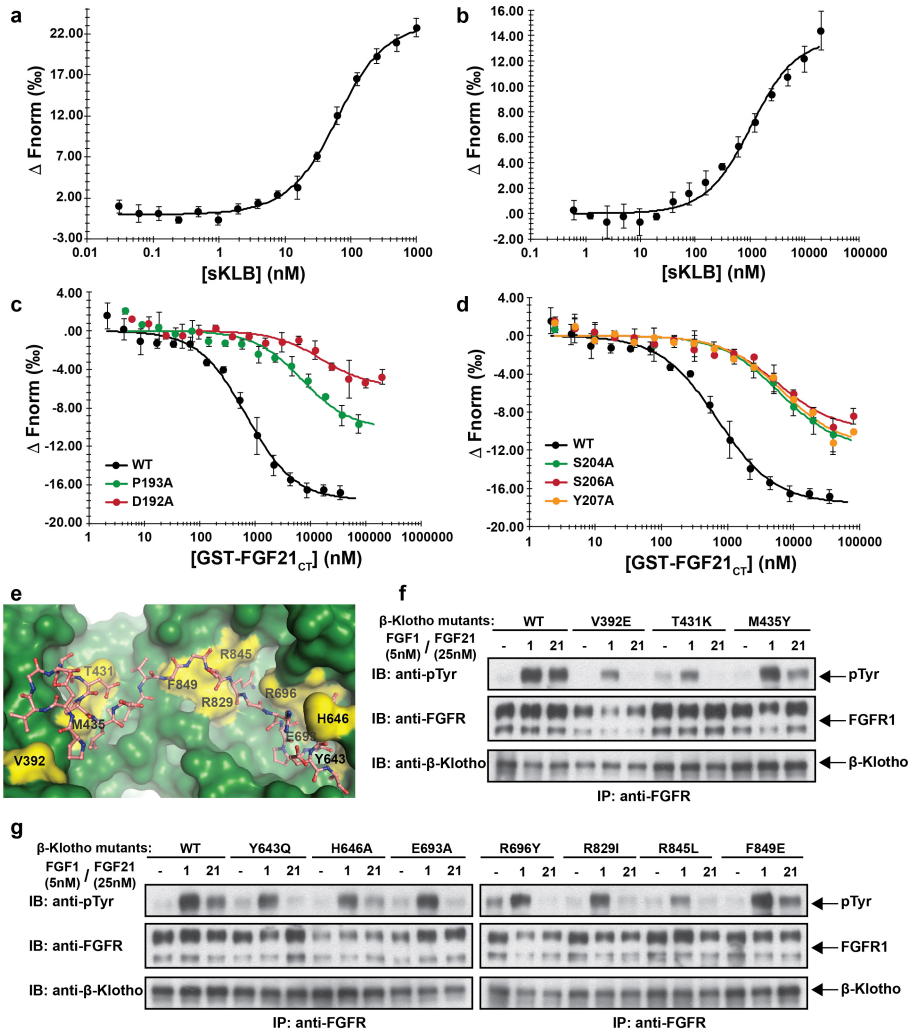

Extended Data Figure 6 | Validation of FGF21-binding interface to β-klotho by ligand-binding and cell-stimulation experiments. **a**, **b**, MST-based binding affinity measurements of (**a**) FGF21 to sKLB (**a**) and FGFR1c$_{D2D3}$ to sKLB (**b**) that yielded $K_d = 43.5 \pm 5.0$ nM and $K_d = 940 \pm 176$ nM, respectively. **c**, **d**, MST-based competition assay with GST–FGF21$_{CT}$ that contained mutations in regions that interact with site 1 (**c**) or site 2 (**d**). Half-maximal inhibitory concentration (IC_{50}) values for wild type, 704 ± 96 nM; D192A, 15,900 ± 6,210 nM; P193A, 7,160 ± 2,350 nM; S204A, 5,990 ± 1,040 nM; S206A, 5,560 ± 1,590 nM; and Y207A, 6,630 ± 1,570 nM. The dots and error bars in panels **a**–**d** denote mean and s.d. of ΔF_{norm} ($n = 3$ independent samples). Individual experimental data are plotted in Extended Data Fig. 9. **e**, Location of mutated amino acid residues (yellow) in sKLB (green) occupied by FGF21 (salmon) that were analysed in **f** and **g**. **f**, **g**, Stably transfected L6 cells co-expressing FGFR1c together with wild-type or β-klotho mutants were stimulated with either FGF21 or FGF1 (control) and analysed for FGFR1c activation by monitoring tyrosine phosphorylation of FGFR1c. Lysates of ligand-stimulated or unstimulated cells were subjected to immunoprecipitation with anti-FGFR1 antibodies, followed by immunoblotting with either anti-pTyr or anti-FGFR1 antibodies.

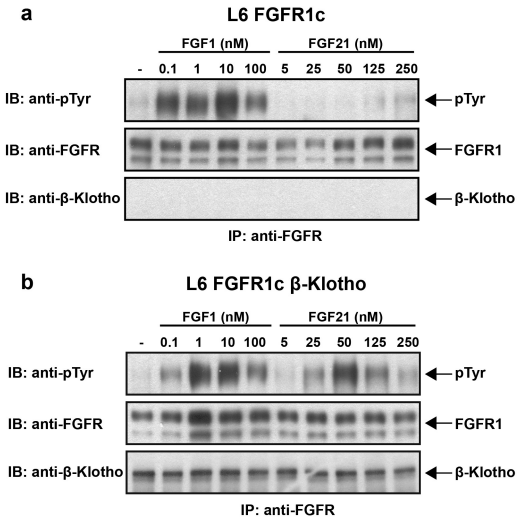

Extended Data Figure 7 | β-Klotho is required for FGFR1c-mediated signalling induced by FGF21. a, **b**, L6 cells that expressed either FGFR1c alone (**a**) or FGFR1c together with β-klotho (**b**) were stimulated with a range of concentrations of FGF1 or FGF21, and phosphotyrosine (pTyr) levels of FGFR were monitored by immunoprecipitation with anti-FGFR1 antibodies, followed by immunoblotting with anti-pTyr antibodies.

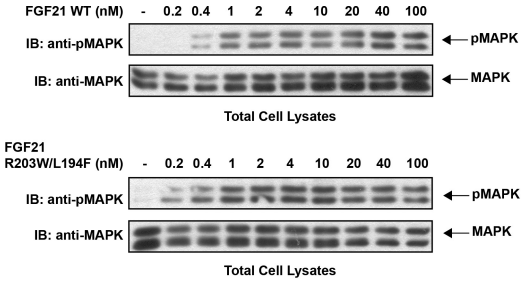

Extended Data Figure 8 | MAP kinase stimulation induced by wild-type or mutant FGF21. L6 cells that co-expressed β-klotho and FGFR1c were stimulated with wild-type FGF21 (top) or FGF21(R203W/L194F) (bottom), and phosphorylation levels of MAP kinase in cell lysates were monitored.

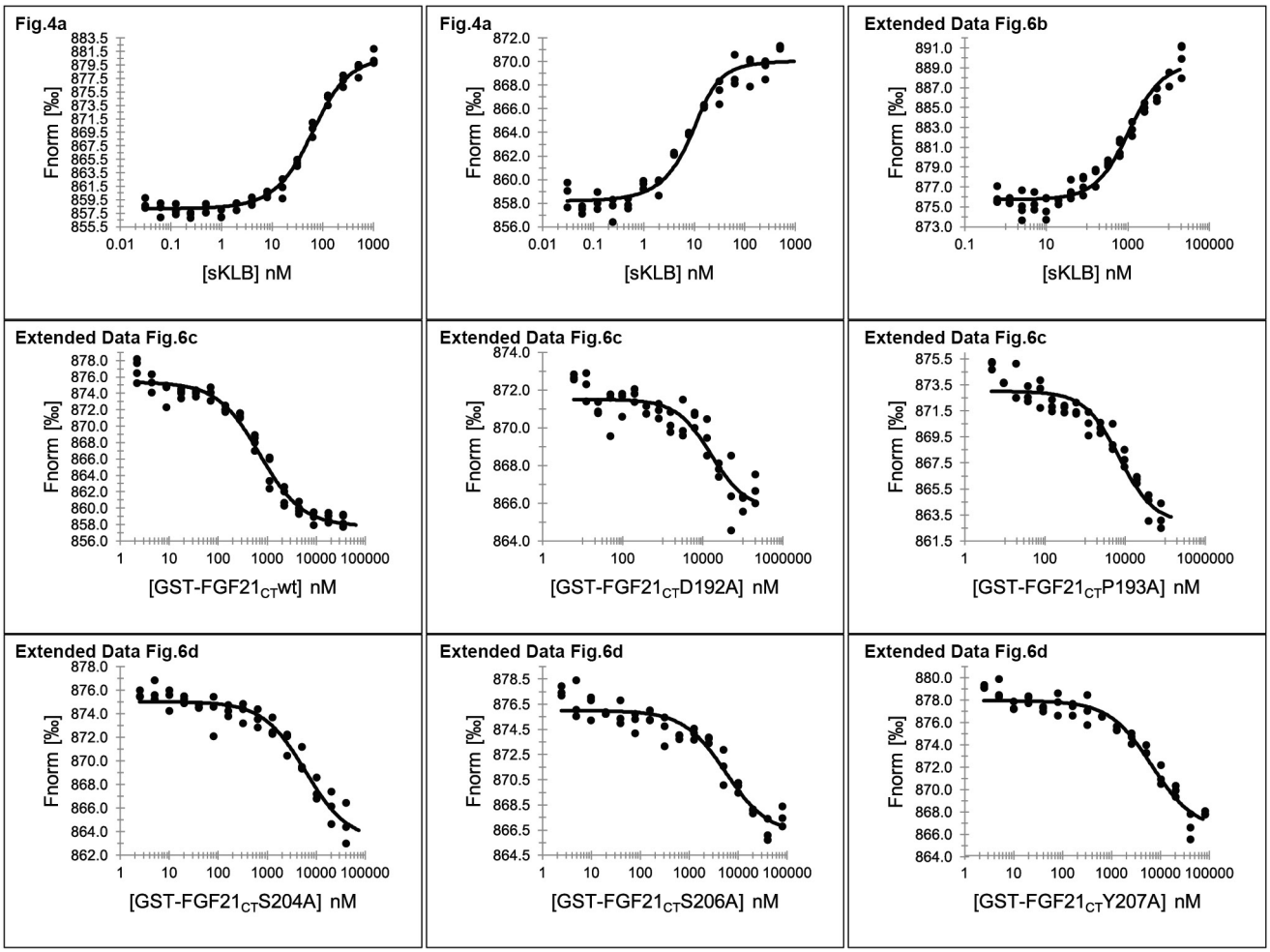

Extended Data Figure 9 | MST data with individual data points. Figures that contain the data are indicated.

Extended Data Table 1 | Crystallographic data collection and refinement statistics

	KLB_{D1}:Nb914	sKLB:Nb914	sKLB:Nb914:$FGF21_{CT}$
Data collection			
Space group	C2	$P2_12_12_1$	$P2_12_12_1$
Cell dimensions			
a, b, c (Å)	229.43, 49.35, 54.31	48.68, 144.07, 215.61	48.65, 145.49, 213.83
α, β, γ (°)	90, 100.22, 90	90, 90, 90	90, 90, 90
Resolution (Å)	41.27-1.70 (1.76-1.70)	47.49-2.20 (2.28-2.20)	60.14-2.61 (2.70-2.61)
R_{merge}	0.0546 (0.441)	0.109 (0.880)	0.0905 (1.289)
$CC_{1/2}$ (%)	99.9 (86.4)	99.7 (76.3)	99.7 (43.1)
<I/σ>	20.36 (2.87)	20.13 (2.71)	13.12 (1.03)
Completeness (%)	98 (87)	100 (97)	98 (96)
Redundancy	4.2 (3.4)	7.1 (6.9)	3.9 (3.3)
Refinement			
Resolution (Å)	41.27-1.70	47.49-2.20	60.14-2.61
No. of reflections used	65178	77784	46521
R_{work} / R_{free} (%)	17.16 / 19.64	18.62 / 21.06	19.11 / 22.89
No. of atoms			
Protein	4453	7731	7874
Ligands	42	125	13
Waters	271	112	0
Average B-factors			
Protein	26.11	43.00	63.42
Ligands	45.67	65.37	68.90
Waters	30.97	39.59	n/a
R.m.s. deviations			
Bond lengths (Å)	0.006	0.008	0.012
Bond angle (°)	0.82	0.95	1.30

nature research

Corresponding author(s): Joseph Schlessinger

☐ Initial submission ☒ Revised version ☐ Final submission

Life Sciences Reporting Summary

Nature Research wishes to improve the reproducibility of the work that we publish. This form is intended for publication with all accepted life science papers and provides structure for consistency and transparency in reporting. Every life science submission will use this form; some list items might not apply to an individual manuscript, but all fields must be completed for clarity.

For further information on the points included in this form, see Reporting Life Sciences Research. For further information on Nature Research policies, including our data availability policy, see Authors & Referees and the Editorial Policy Checklist.

Experimental design

1. Sample size

Describe how sample size was determined.	No sample size calculation was performed

2. Data exclusions

Describe any data exclusions.	No data was discarded

3. Replication

Describe whether the experimental findings were reliably reproduced.	All binding and cellular experiments were successfully reproduced at least three times.

4. Randomization

Describe how samples/organisms/participants were allocated into experimental groups.	Sample randomization is not relevant to our study as structural analysis does not involve randomization.

5. Blinding

Describe whether the investigators were blinded to group allocation during data collection and/or analysis.	Binding is not relevant to studies involving biochemical and structural analyses as animals and/or human subjects are not utilized.

Note: all studies involving animals and/or human research participants must disclose whether blinding and randomization were used.

6. Statistical parameters

For all figures and tables that use statistical methods, confirm that the following items are present in relevant figure legends (or in the Methods section if additional space is needed).

n/a	Confirmed	
☐	☒	The exact sample size (*n*) for each experimental group/condition, given as a discrete number and unit of measurement (animals, litters, cultures, etc.)
☐	☒	A description of how samples were collected, noting whether measurements were taken from distinct samples or whether the same sample was measured repeatedly
☐	☒	A statement indicating how many times each experiment was replicated
☒	☐	The statistical test(s) used and whether they are one- or two-sided (note: only common tests should be described solely by name; more complex techniques should be described in the Methods section)
☒	☐	A description of any assumptions or corrections, such as an adjustment for multiple comparisons
☒	☐	The test results (e.g. *P* values) given as exact values whenever possible and with confidence intervals noted
☐	☒	A clear description of statistics including central tendency (e.g. median, mean) and variation (e.g. standard deviation, interquartile range)
☐	☒	Clearly defined error bars

See the web collection on statistics for biologists for further resources and guidance.

Software

Policy information about availability of computer code

7. Software

Describe the software used to analyze the data in this study.	X-ray data processing and structure determination was performed using HKL2000, XDS, Phenix, Phaser, Coot and PyMOL Molecular Graphics System.

For manuscripts utilizing custom algorithms or software that are central to the paper but not yet described in the published literature, software must be made available to editors and reviewers upon request. We strongly encourage code deposition in a community repository (e.g. GitHub). *Nature Methods* guidance for providing algorithms and software for publication provides further information on this topic.

Materials and reagents

Policy information about availability of materials

8. Materials availability

Indicate whether there are restrictions on availability of unique materials or if these materials are only available for distribution by a for-profit company.	A variety of materials were purchased from commercial vendors and unique material are described and available without restrictions.

9. Antibodies

Describe the antibodies used and how they were validated for use in the system under study (i.e. assay and species).	anti-betaKlotho antibody was purchased from R&D Systems (cat.# AF5889 anti-phosphotyrosine antibody, 4G10, was purchased from Millipore (cat.# D5-1050). Validation info for commercial antibodies is available on the manufacturer's websites. Rabbit polyclonal anti-FGFR1 antibody was obtained by immunizing with a peptide that has the sequence of C-terminal 18 amino acid of FGFR1 and validated through western blot analysis in our laboratory.

10. Eukaryotic cell lines

a. State the source of each eukaryotic cell line used.	HEK293Ebna and L6 cells were obtained from ATCC.
b. Describe the method of cell line authentication used.	Cells used for transfection were not authenticated.
c. Report whether the cell lines were tested for mycoplasma contamination.	All cell lines tested negative for mycoplasma contamination.
d. If any of the cell lines used are listed in the database of commonly misidentified cell lines maintained by ICLAC, provide a scientific rationale for their use.	No commonly misidentified cell lines were used.

Animals and human research participants

Policy information about studies involving animals; when reporting animal research, follow the ARRIVE guidelines

11. Description of research animals

Provide details on animals and/or animal-derived materials used in the study.	No animals were used.

Policy information about studies involving human research participants

12. Description of human research participants

Describe the covariate-relevant population characteristics of the human research participants.	The study did not involve human research participants.